Published in final edited form as:
J Mol Biol. 2010 March 26; 397(2): 408–422. doi:10.1016/j.jmb.2010.01.030.

Resonance Assignment and Three-Dimensional Structure Determination of a Human Alpha-Defensin, HNP-1, by Solid-State NMR

Yuan Zhang[1], **Tim Doherty**[1], **Jing Li**[2], **Wuyuan Lu**[2], **Cyril Barinka**[3], **Jacek Lubkowski**[3], and **Mei Hong**[1,*]

[1]Department of Chemistry, Iowa State University, Ames, IA, 50011

[2]Institute of Human Virology, Institute of Human Virology & Department of Biochemistry and Molecular Biology, University of Maryland School of Medicine, Baltimore, MD, 21201

[3]Macromolecular Crystallography Laboratory, National Cancer Institute, Frederick, MD, 21702

Abstract

Human α-defensins (HNPs) are immune defense mini-proteins that act by disrupting microbial cell membranes. Elucidating the three-dimensional structures of HNPs in lipid membranes is important for understanding their mechanisms of action. Using solid-state NMR, we have determined the three-dimensional structure of HNP-1 in a microcrystalline state outside the lipid membrane, which provides benchmarks for structure determination and comparison with the membrane-bound state. From a suite of 2D and 3D magic-angle spinning experiments, ^{13}C and ^{15}N chemical shifts were obtained that yielded torsion angle constraints while inter-residue distances were obtained to restrain the three-dimensional fold. Together, these constraints led to the first high-resolution SSNMR structure of a human defensin. The SSNMR structure has close similarity to the crystal structures of the HNP family, with the exception of the loop region between the first and second β-strands. The difference, which is partially validated by direct torsion angle measurements of selected loop residues, suggests possible conformational variation and flexibility of this segment of the protein, which may regulate HNP interaction with the phospholipid membrane of microbial cells.

Keywords

Human α-defensin; solid-state NMR; resonance assignment; structure determination; antimicrobial peptides

Introduction

Antimicrobial peptides (AMPs) are small cationic peptides that constitute part of the innate immune system of many plants and animals to rapidly kill invading microbial pathogens. In mammals the two main classes of antimicrobial peptides are cathelicidins and defensins 1.

* Corresponding author: Department of Chemistry, Iowa State University, Ames, IA, mhong@iastate.edu, Tel: 515-294-3521, Fax: 515-294-0105 .

While most cathelicidins are α-helical in structure, defensins contain β-strands stabilized by three disulfide bonds [2-4]. Based on the disulfide-linkage patterns, three classes of defensins, α-, β-, and θ-defensins, are identified in vertebrates. Humans have six α-defensins that contain 29-32 residues. Four of these proteins are present in the azurophilic granules of neutrophils and are called human neutrophil peptides 1-4 (HNP 1-4) [2; 5], and two are expressed in intestinal Paneth cells and are called HD-5 and HD-6 [6; 7]. Except for HD-6, all five human α-defensins have wide-spectrum antimicrobial activities with LD_{50} in the μg/ml range [8; 9]. Similar to most other AMPs, the main mechanism of action of HNPs is believed to be permeabilization of the microbial cell membrane [10; 11].

The presence of three antiparallel disulfide-stabilized β-strands makes defensins larger and more complex proteins than most other AMPs. In particular, they are natural extensions of the two-stranded β-hairpin AMPs such as protegrins from porcine leukocytes and tachyplesins from horseshoe crabs, whose membrane-bound structure and lipid interaction have been characterized in detail by solid-state NMR recently [12-21]. Compared to these smaller β-sheet AMPs, HNPs have weaker antimicrobial activities. Moreover, although HNP 1-3 have nearly identical sequences, differing only in the N-terminus residue, their activities differ by as much as 4-fold [8]. Understanding the activity differences among human defensins requires structural investigations in the lipid membrane. However, so far most high-resolution structures of human defensins come from X-ray crystallography in the absence of any membrane-mimetic solvents [3; 4]. A few biophysical studies that investigated the interactions of defensins with lipid membranes have also been reported, but did not contain high-resolution structural information [22-24].

Solid-state NMR magic-angle spinning (MAS) NMR has been recently shown to be able to elucidate the atomic-resolution structure of ^{13}C, ^{15}N-labeled proteins in microcrystalline states [25-28], in fibrillar forms [29-31], and in lipid membranes [32; 33]. A wide variety of 2D and 3D correlation techniques have been developed to obtain resonance assignment [34; 35], torsion angles [36-38] and inter-atomic distances [39]. Therefore, the technology is now in place to determine the full structures of human α-defensins in lipid membranes to elucidate the mechanism of action of this important class of immune defense molecules.

In this work, we report the three-dimensional structure determination of recombinant HNP-1, whose sequence is shown in Figure 1, by SSNMR. We have carried out resonance assignment and internuclear distance measurements of HNP-1 in an ordered microcrystalline state, in preparation for structure determination of the protein bound to the lipid membrane, since membrane-bound proteins usually give lower-resolution spectra due to the disorder created by the lipid bilayer. The conformation of microcrystalline HNP-1 also represents the protein structure before binding to the lipid membrane, and is thus necessary for understanding potential conformational changes of HNPs induced by the lipid bilayer. We compare the SSNMR structure with various published crystal structures of HNPs [3; 4; 40].

Results

Preparation of microcrystalline HNP-1 samples for solid-state NMR experiments

The solid-state NMR data presented here were obtained from microcrystalline samples of HNP-1 precipitated from a polyethylene glycol (PEG) solution. Two samples were prepared using different concentrations of the protein stock solution. The high-concentration stock solution (36 mg/ml) yielded microcrystals one hour after mixing with PEG, while the low-concentration stock solution (30 mg/ml) produced microcrystals gradually in a 4-day period, with ~80% of the protein eventually precipitating from the supernatant. The slower precipitation produced larger crystals of ~20 μm diameter compared to 2 μm for the rapidly

precipitated sample. Figure 2 shows an image of HNP-1 microcrystals obtained from the slower precipitation procedure.

Both microcrystalline HNP-1 samples yielded well-resolved ^{13}C and ^{15}N MAS spectra, shown in Figure 3. For the rapidly precipitated sample in the 4 mm rotor, the ^{13}C full widths at half maxima were 0.6 – 1.0 ppm and the ^{15}N linewidths were 1.3 – 1.7 ppm. For the slowly precipitated sample in the 2.5 mm rotor, the linewidths improved to 0.4 – 0.8 ppm for ^{13}C and 1.0 – 1.5 ppm for ^{15}N. Faster spinning frequencies and stronger ^{1}H decoupling fields further contributed to the narrower linewidths of the 2.5 mm rotor sample.

Resonance assignment of HNP-1 by 2D and 3D SSNMR

We first assigned the amino acid spin systems of HNP-1 using 2D ^{13}C-^{13}C correlation experiments, including a DARR experiment with 40 ms mixing, and double-quantum (DQ)-filtered experiments using SPC5 [41] and CM5RR sequences 42. The 40 ms DARR spectrum allowed the assignment of most amino acid types (Figure 4a, b, d), including Cys, Ala, Ile, Arg, Leu, Pro, and Thr, which have distinct cross peak patterns. The aromatic residues were assigned based on the Cα/Cβ cross peaks to the aromatic carbons. For example, the Cγ of the unique tryptophan W27 resonates at 107.8 ppm (Figure S1), which allowed the rest of the W27 spin system to be identified. For the unique glutamate E14 and glutamine Q23, the sidechain Cδ chemical shifts (181 ppm for E14 and 176 ppm for Q23) served as useful guides for identifying the chemical shifts of the other sidechain carbons.

The DQ-filtered 2D spectra confirmed the DARR assignment by exhibiting opposite intensities for one-bond and two-bond cross peaks. For example, Gly Cα and Cys Cβ, which both resonate at 40-45 ppm, are distinguished based on the negative intensities of the one-bond Gly Cα-CO peaks and the positive intensities of the two-bond Cys Cβ-CO peaks in the CM_5RR spectra (Figure 4c, e, f). Similarly, while Q23 Cβ has similar chemical shifts to Arg Cγ in the DARR spectrum, in the DQ filtered spectra Q23 Cβ exhibits a positive one-bond Cα-Cβ cross peak, which is distinct from the negative two-bond Arg Cα-Cγ cross peaks. By comparing various 2D ^{13}C-^{13}C spectra, we assigned all amino acid spin systems except for one Arg.

Next, we obtained sequence-specific assignment from inter-residue NCOCX and intra-residue NCACX 3D experiments [34; 35]. Figure 5 shows a representative strip of F2-F3 planes of the two 3D experiments for residues G18-Q23. We first identified the ^{15}N chemical shift of residue *i* in the NCACX spectrum by comparing the ^{13}C chemical shifts with those obtained from the 2D CC spectra. The ^{15}N chemical shift of residue *i*+1 was then obtained from the NCOCX spectrum through its cross peaks with the ^{13}C chemical shifts of residue *i*. The ^{15}N plane of residue *i*+1 was then searched in the NCACX spectrum to identify the ^{13}C chemical shifts of residue *i*+1.

A2, A9, T19 and C30 are clear starting points for assigning a consecutive segment of residues. The N-terminal residue A2 has a distinct ^{15}N chemical shift of 41.7 ppm, which is folded to 106.9 ppm. Residue A9 has cross peaks with P8, which has characteristic ^{13}C chemical shifts. Residue T19 has characteristic Cα and Cβ chemical shifts.

The four Ala residues, which are well resolved in the 2D CC spectra, were sequentially assigned in the 3D spectra. For example, A9 was assigned based on its correlation with the unique P8 and with C10, and A12 was assigned based on its correlation with the well defined I11 and G13. For the three Gly residues, G24 was identified by inter-residue correlations Q23N-G24Cα and R25N-G24Cα in the 3D spectra and in the 100 ms DARR spectrum, while G18 was assigned based on the T19N-G18Cα correlations in the 3D spectrum.

The six Cys residues were resolved and assigned based on their cross peaks with their neighboring residues in the NCOCX spectrum. For example, C3 has characteristic cross peaks with A2 Cβ and Cα, and C5 has cross peaks with the Y4 spin system. Interestingly, C5 exhibits two Cβ chemical shifts differing by 0.9 ppm, suggesting the presence of two conformations at this site. C10 has a Cβ chemical shift of 33.4 ppm (on the TMS scale), which is slightly low for an oxidized cysteine. However, its assignment was corroborated by multiple sequential C10 – A9 cross peaks and I11 – C10 cross peaks. For example, C10N-A9C'-A9C /C cross peaks were identified in the 3D NCOCX spectrum, and sequential C10C'- A9CÛ, C10Cÿ- A9CÛ, and A9C - C10C cross peaks were also detected in the 100 ms DARR spectrum (Figure S2).

The complete ^{13}C and ^{15}N isotropic chemical shifts of HNP-1 are summarized in Table 1. Among the six cysteines, the C10 – C30 pair has relatively upfield Cβ chemical shifts. To further verify that C10 and C30 are indeed disulfide-bonded, we compared the Cα and Cβ chemical shifts of all HNP-1 cysteines with literature statistical analyses of the dependence of cysteine ^{13}C chemical shifts on the oxidation state and conformation [43; 44]. On the DSS scale, the oxidized cysteines have Cβ chemical shifts of 33 - 51 ppm and Cα chemical shifts of 50 - 61 ppm. When the HNP-1 cysteine chemical shifts are also referenced to DSS (thus increasing the ^{13}C chemical shifts in Table 1 by 1.7 ppm), we find that all six cysteines, including C10 and C30, lie in the oxidized range (Figure S3), thus confirming the disulfide-bonded nature of all three pairs.

Backbone dihedral angles and verification by dipolar correlation experiments

The ^{13}C and ^{15}N chemical shifts allowed us to determine the backbone (φ, ψ) torsion angles of HNP-1 using the well-known empirical relation between N, Cα, Cβ, CO chemical shifts and protein secondary structure 45. We used the TALOS program 46 to predict the (φ, ψ) angles and compared them with the values found from the crystal structure of HNP-3 3 (PDB code: 1DFN). The chemical-shift constrained torsion angles indicate three well-defined β-strands, β1, β2 and β3, separated by a type-II β-turn at A12-G13 and a type I' β-turn at Q23-G24 (Figure 6). These secondary structure motifs are consistent with those of the HNP-3 structure, although the boundaries of the loop or turn segments between β-strands differ slightly between HNP-3 and HNP-1.

Among the 28 (φ, ψ) pairs predicted by TALOS, excluding the terminal A2 and C31, 24 φ angles and 24 ψ angles agree well with the crystal structure values within the experimental uncertainty. Residues with large dihedral angle discrepancies are P8, C10, Y17, G18 and Y22 (Figure 6 and Table S1). P8 and C10 both lie in the loop between β1 and β2 strands and might be expected to be dynamically disordered. However, the HNP-3 crystal structure shows well-defined positions for these residues, with B factors not higher than the average [3]. Direct measurement of C-H order parameters of the HNP-1 sample by NMR (see Figure 11 below) also indicates that the loop region in HNP-1 is not dynamic.

To verify the torsion angle differences between TALOS and the crystal structure, we conducted the HNCH experiment to directly measure the φ angles of C10 and Y22. The experiment measures the φ_H angle (defined as H^N-N-Cα-Hα, which is related to φ by $\varphi_H+60°=\varphi$) by correlating the N-H and Cα-Hα dipolar couplings [36; 47], and is particularly sensitive to the β-sheet conformation, which has φ_H angles around 180°. To maximize the angular resolution, we implemented the N-H doubled version of the experiment [47]. In principle, a 3D experiment where two chemical shift dimensions provide site resolution while one dipolar dimension gives the angular information is the most desirable. However, the low sensitivity of the 3D experiment and the limited protein amount precluded its implementation. Thus, we used one ^{13}C chemical shift dimension for site resolution and measured the dipolar evolution at time 0 and half a rotor period. Simulations have shown that the HNCH dipolar dephasing at the middle of the rotor period is the most sensitive to φ_H angle differences [48].

Figure 7c shows the Cα region of the ^{13}C spectra with 0 and half a rotor period of HNCH evolution. The peaks were assigned based on the 2D and 3D spectra above. Although single-site resolution is not available, most sites have consistent φ angles between the TALOS prediction and the crystal structure within ±10° (Table S1). The only uncertain residues are C10 and Y22, thus their φ_H angles can be extracted from the intensities. Specifically, the C10 Cα signal at 50.8 ppm overlaps with only one residue, A28, whose φ_H angle is −145°±5°, as indicated by both TALOS and the crystal structure (Figure 7b). Thus, the calculated HNCH curve for 50.8 ppm is very sensitive to the C10 φ_H angle (Figure 7d). The experimental intensity (0.53) is much more consistent with the TALOS prediction of a β-sheet like φ_H angle of about 180° rather than a low value of about −130° (Figure S4). Similarly, the measured HNCH intensity for the 54.5-ppm peak, which is a composite of Y22 Cα with five other Cα sites, is more consistent with the TALOS prediction than with the crystal structure, although the distinction between the two possibilities is smaller for this peak due to more resonances overlapping at this position.

For P8, both φ and ψ angles differ between the chemical shift prediction and the crystal structure (Table S1). The lack of H^N at Pro precludes direct measurement of its φ angle. In principle, the ψ angle can be measured using the NCCN technique [37]. At present the protein amount is insufficient for this experiment, which requires ^{13}C double-quantum filtration in addition to ^{13}C-^{15}N REDOR. Thus, future experiments are necessary to clarify the conformational discrepancy at P8. Nevertheless, based on distance constraints involving this loop, we hypothesize that the difference may be real instead of due to inaccuracy of the NMR structure determination (see below).

The torsion angle difference for Y17-G18 is also noteworthy. TALOS predicted a relatively ideal β-strand ψ angle for Y17 whereas the crystal structure gives an unusual ψ angle near 0°. On the other hand, the TALOS Y17 torsion angles have relatively large uncertainties (ΔΦ=23°, ΔΨ=20°) (Table S1). Among the 10 pairs of torsion angles predicted, seven pairs lie in the β-sheet region while three pairs lie near the α-helical region, with ψ angles of about −20°, which are similar to the crystal structure ψ value. Thus, the ensemble of NMR torsion angles for Y17 encompasses the crystal structure value.

For G18, chemical shifts predicted a φ angle of −120° whereas the crystal structure shows a φ angle near 180°. Since glycine residues have two Hα protons, the HNCH experiment is not ideal for measuring their φ angles. The TALOS uncertainties for G18 are (Δφ=35°, Δψ=23°) (Table S1), and three of the predicted pairs of angles lie in the right-handed α-helix region of the Ramachandran diagram. Thus, the conformation of this residue is not well predicted from the chemical shifts. On the other hand, G18 is strictly conserved in all human defensins. Based on comparisons of HNP-4, HD5 and HD6 crystal structures, it has been suggested that G18 may act as a hinge for the G18-L29 β-hairpin [4], which has significantly different orientations in various HNPs. Thus, it remains a possibility that the G18 torsion angle difference between the NMR and crystal structures may reflect real conformational variations at this residue.

Inter-residue distances

To constrain the three-dimensional fold of HNP-1, we measured distances between sequential and non-sequential residues using DARR experiments with long mixing times. Two spin diffusion mixing times, 100 ms and 200 ms, were chosen, which resulted in larger numbers of cross peaks that deteriorated the spectral resolution (Figure 8). To bypass this problem, we used a comparative strategy to identify the long-distance correlation peaks. For each inter-residue cross peak, we first found all possible assignments that agree with the peak position to ±0.2 ppm. We then measured the distances of these inter-residue pairs in the HNP-3 crystal structure [3], and selected the assignment with the shortest distance. For these inter-residue cross

peaks, since distances between sequential residues are usually the shortest, where ambiguity arises, we gave preferences to sequential distances over medium or long-range distances.

In this way, we identified 40 inter-residue CC correlations, among which 26 were sequential contacts, 1 was medium range ($1< |i-j| <4$), and 13 were long-range contacts ($|i-j| > 4$). Non-sequential correlations were observed for residues A2, Y4, R6, I7, C10, E14, R16, I21, L26, W27, F29 and C30 (Table 2). Six long-range correlation peaks were detected between β1 and β3 strands, and six contacts between β2 and β3 strands. These inter-strand correlations provided important restraints to the three-dimensional fold of the protein.

We also measured a 2D ^{15}N-^{15}N correlation spectrum to obtain additional inter-residue distance restraints (Figure 9). The Gly region was the best resolved and provided many useful sequential and long-range cross peaks. P8 also gave well-resolved cross peaks due to its unique imine ^{15}N chemical shift. The 110 – 130 ppm region is more congested, thus we only assigned the intensity maxima and gave them tentative assignments in the same fashion as the CC constraints. The non-sequential NN contacts are included Table 2.

Since the above distance extraction strategy used the HNP-3 structure as partial input, potential differences of HNP-1 from HNP-3 can only be discerned based on missing correlations for HNP-1, and mis-assignment cannot be ruled out. To extract distance restraints in a *de novo* fashion, without input from the HNP-3 structure, we carried out further 3D ^{13}C-^{13}C-^{13}C correlation experiments, which removed the problem of resonance overlap. As we report in a separate publication, the 3D CCC experiment yielded 270 unique inter-residue distances, among which 129 were sequential, 45 were medium range, and 96 were long-range constraints. These distances verified and refined the current structure, as we show below.

Three-dimensional structure of HNP-1

Using the distance and angular restraints obtained from the above SSNMR experiments, we calculated the HNP-1 structure using the XPLOR-NIH program. We assigned the distance restraints to specific ranges based on the mixing times for the first appearance of cross peaks that correspond to well-defined secondary structures (Table 3). Sequential Cα-Cα distances are fixed by the peptide plane geometry to be 3.8 Å and were thus placed in the range of 3.5-4.1 Å. Sequential N-N distances depend on the ψ torsion angle and fall within the range of 2.5 – 3.6 Å. All inter-residue peaks first observed in the 100 ms ^{13}C-^{13}C DARR spectrum were assigned to the range 2.5 – 5.4 Å, those first appearing in the 200 ms DARR spectrum assigned to 2.5 – 6.3 Å, and those inter-residue peaks appearing in the 2D CHHC spectra assigned to 2.5 – 7.5 Å. In addition, the few inter-residue correlations observed in the 40 ms ^{13}C-^{13}C DARR spectrum were assigned to the range 2.5 – 4.8 Å. All non-sequential ^{15}N-^{15}N contacts were placed in the 3.0 – 6.0 Å range.

In total, we obtained 60 inter-residue distance restraints, 56 (φ, ψ) torsion angles, and three disulfide bond restraints, and subjected them to structure calculation by XPLOR-NIH. The 10 lowest-energy structures out of 200 calculated structures (Figure 10a) cluster closely. Compared to the crystal structure, the average NMR structure has a backbone atomic root-mean-square deviation (RMSD) of 2.7 Å and a heavy-atom RMSD of 3.8 Å. Figure 10 compares the NMR structure ensemble with the X-ray structure of HNP-3. The NMR structure shows three well-defined β-strands connected by a long loop between the β1 and β2 strands and a tight turn between the β2 and β3 strands. Both the HNP-1 NMR structure and the HNP-3 crystal structure have the same topology: the β3 strand is inserted between the β1 and β2 strands. Beyond these similarities, we found two main differences: the β1-β2 loop has a very different orientation to the rest of the protein in the two structures, and the β2 strand has a different twist and orientation. The origins of these differences will be discussed below.

To ascertain whether large-amplitude motion exists in the HNP-1 backbone, we measured the ^{1}H-^{13}C one-bond dipolar couplings using a 2D LG-CP experiment (Figure 11). The spectrum shows that most backbone Cα sites have rigid-limit couplings of ~12.5 kHz after scaling by the homonuclear decoupling scaling factor. The only exception is the signal at 56 ppm, which shows a splitting of 9.8 kHz. This value corresponds to a smaller C-H order parameter of 0.78, consistent with moderate-amplitude dynamics of some of the Cα sites, including I7, Y17, and F29.

Discussion

HNP-1 conformational homogeneity and SSNMR structural quality

The microcrystalline HNP-1 samples are well ordered on the nanometer and micrometer scale. The ^{13}C linewidths of 0.4 – 0.8 ppm and ^{15}N linewidths 1.0-1.5 ppm are overall comparable to those observed in other microcrystalline proteins [49] and are better than some amyloid proteins [31]. The ^{15}N linewidths are particularly sensitive to the conformational heterogeneity. Compared to one of the well-studied globular proteins, ubiquitin [49], whose ^{15}N linewidths were reported as 0.3 – 0.5 ppm, the microcrystalline HNP-1 still has residual conformational heterogeneity. However, since the eventual goal is to study HNP-1 in the lipid membrane, whose thermal disorder generally promotes conformational heterogeneity in small proteins, it is not essential to produce HNP-1 with the highest conformational homogeneity.

Variable-temperature 1D ^{13}C and ^{15}N spectra showed quantitatively similar intensities and linewidths in the range of 293 – 253 K (Figure S5), indicating that the HNP-1 backbone is largely immobilized at room temperature and only small-amplitude segmental motions exist. This observation is supported by the 2D LG-CP spectrum, which exhibits near rigid-limit Cα - Hα dipolar couplings for most sites. The persistence of narrow linewidths at mild low temperatures is consistent with the behavior of other microcrystalline proteins but contrasts with that of membrane peptides, which manifest gel-phase-induced line broadening in the same temperature range.

The quality of the HNP-1 structure can be compared with the SSNMR structures of other recently studied globular proteins, such as the α-spectrin SH3 domain 25, ubiquitin 26, and GB1 [50]. In terms of agreement with the crystal structure, the SH3 domain and HNP-1 are comparable: the SH3 domain NMR structure has a backbone RMSD of 2.6 Å from the crystal structure for the β-strand segments, while the HNP-1 NMR structure has an all-segment backbone RMSD of 2.7 Å from the crystal structure of HNP-3. However, this similarity belies the difference that a larger number of restraints were obtained (292) for SH3, which corresponded to ~5 restraints per residue, and all constraints were independently extracted from NMR. In comparison, 116 restraints were obtained for HNP-1, thus about 4 restraints were available per residue. The HNP-1 structure constraints also contain a smaller number of medium and long-range distances (24) compared to SH3 (170 non-sequential restraints).

For ubiquitin, structure determination using a combination of uniformly ^{13}C-labeled protein and 2-^{13}C selectively labeled protein resulted in 336 inter-residue contacts for the 76-residue protein [49], among which 149 were sequential, 74 were medium range and 113 were long range. Combined with 122 torsion angle restraints, the high-resolution solid-state NMR structure had a □1 Å RMSD for secondary structure elements compared to the crystal structure. For the 56-residue GB1, a very high resolution NMR structure was obtained from 888 unique distance restraints and dihedral angles, resulting in a backbone RMSD of 1.32 Å from one of the crystal structures [50].

Conformation of the inter-strand β1-β2 loop and comparison with other human α-defensins

Compared to the structures of other human α-defensins [4], the HNP-1 NMR structure has the same overall fold, with three antiparallel β-strands arranged into a β-sheet. A tight β-hairpin connects β2 and β3 strands while a loop connects the β1 and β2 strands, so that the N- and C-termini lie close together. This structural fold separates the charged and hydrophobic regions spatially, thus may facilitate the insertion of the protein into the phospholipid bilayer with the hydrophobic region buried in the membrane interior while the charged region interacting with the polar surface of the bilayer and with water [3].

Within the context of this general similarity, the SSNMR structure of HNP-1 shows two main differences from the crystal structures of various HNPs. First, the β2 strand in the NMR structure has less orientation change between the N- and C-terminal half compared to the crystal structure (Figure 10b, c), and the strand twist is also less significant. We attribute these differences largely to insufficient distance restraints between the β2 strand and the rest of the protein (9 distances for 7 residues). When the much larger number of inter-residue distances restraints from the 3D CCC experiment were used for structure calculation, the β2 strand was found to have a more similar twist and orientation to those of the HNP-3 structure. Thus, there appears to be no real conformational difference in the β2 strand of HNP-1 and HNP-3.

The second, more important, difference is the conformation of the loop between residues I7 and R15, which controls the relative orientation of the β1 and β2 strands. In the HNP-3 structure, the loop is bent at P8-A9 and protrudes significantly from the rest of the protein, while in the HNP-1 structure, the P8-A9 segment is extended and the loop is tugged closer to the β2 strand (Figure 10d). Several lines of evidence suggest that these are real conformational differences between HNP-1 and HNP-3, rather than artifacts due to insufficient constraints of the NMR structure. The structural inputs for the loop region include the chemical-shift based torsion angles (Table S1) and eleven inter-residue distances (Table 2). The P8 and C10 torsion angles were the main factor that determined the presence or absence of a turn at this position. Although we have not directly measured the P8 ψ torsion angle due to sensitivity limitations, the fact that the C10 φ angle is confirmed by HNCH experiments to have a regular β-strand value suggests that there is a significant possibility that the P8-C10 segment in HNP-1 does not adopt a turn conformation as in HNP-3. Second, eleven inter-residue distances established close contacts between the N-terminal region of the loop (residues I7-P8) and the β3 strand (residues L26-W27), between residue C10 and residues G13-E14 within the loop, and between the end of the loop (residues E14-R15) and the β3 strand (residues F29-C30) (Table 2). Thus, this segment has a reasonable number of distance restraints. When the larger number of independently assigned restraints from 3D CCC experiments were inputted for structure calculation, the loop conformational difference largely remained (Figure 10d), supporting the hypothesis that the conformational difference is real.

It is noteworthy that a previous ^{1}H solution NMR structure of HNP-1 also concluded a different loop orientation [51]. Similar to the current result, the solution structure showed the HNP-1 loop to be well defined by itself but that its relation to the rest of the protein was different from that of HNP-3. Moreover, when the HNP-1 solution structure was compared with the structures of the related rabbit defensins NP-2 and NP-5, it was revealed that the loop conformation also differs among these three proteins. Thus, the solution NMR study suggested that the β1-β2 loop conformation may be highly sequence-specific and may play a systematic role in regulating the activities of different α-defensins.

What might be the origin of the loop conformation difference between HNP-1 and HNP-3? It cannot result from fast motion, since the 2D LG-CP spectrum (Figure 11) shows nearly rigid-limit C-H dipolar couplings and ^{13}C variable-temperature spectra (Figure S5) also indicate little temperature dependence. Thus, this conformational difference must be attributed to

intrinsic structural differences caused either by the single-residue change at the N-terminus or by external environmental factors such as the ionic content, hydration level, and intermolecular packing. Since the loop conformation difference was also seen in the solution NMR structure [51] where there was no crystal packing effects or hydration problems, the single-residue difference at the N-terminus is likely the main reason for the loop conformational variability. The N-terminus residue is Ala in HNP-1, Asp in HNP-3, and absent in HNP-2, which thus starts its sequence with Cys. Thus, HNP-3 is more polar than HNP-1 or HNP-2 at the N-terminus. Correspondingly, the antimicrobial activities of HNP-1 and HNP-2 are similar but the HNP-3 activity is distinct [2]. A recent study of HNP 1-3 against a panel of six bacteria of both Gram-positive and Gram-negative origins showed that the average LD_{50} of HNP-2 is 1.10 ±0.25 times that of HNP-1 [8], indicating very similar potencies, while the average LD_{50} of HNP-3 is 2.20 ± 1.10 that of HNP-1, indicating that HNP-3 is about 2-fold less active than HNP-1 [8]. Molecular dynamics simulations comparing the HNP 1-3 structures suggested that Asp_2 in HNP-3 may facilitate electrostatic interactions between the two monomers of the dimer, thus making the basket-shaped dimer more compact for HNP-3 than for HNP-1 and 2 [52]. This difference may in turn cause distinct interactions of HNPs with the lipid membrane.

Whatever the exact molecular reason for the loop conformation difference, given the tight structural constraints imposed by the disulfide bonds and the dominant β-strand motifs for these proteins, one would expect that it is precisely the non-strand residues, without backbone hydrogen bonds, that should modulate the interactions of these proteins with the lipid membrane and tune their antimicrobial activities. Indeed, preliminary spectra of membrane-bound HNP-1 containing site-specific isotopic labels showed that A12 in the loop undergoes an interesting chemical shift change between a more helical conformation and the conformation seen in the microcrystalline state (Figure S6). This data suggests that the β1-β2 loop conformation is sensitive to the environment, in addition to the sequence. Further comparative structural studies are necessary to fully understand the structure-activity relationship of the HNPs and elucidate the functionally relevant conformation of the β1-β2 loop. Solid-state NMR experiments that determine the conformation, orientation and depth of insertion of HNP-1 in lipid bilayers will be crucial for this purpose.

Materials and Methods

HNP-1 expression and microcrystalline sample preparation

Recombinant HNP-1, whose amino acid sequence is shown in Figure 1, was obtained as a cleavage product from its precursor protein, proHNP1, which was expressed as a GST-fusion protein in *E. coli* and folded. Uniformly ^{13}C, ^{15}N-enriched media Spectra 9 (Cambridge Isotope Laboratories) was used to label the protein. Briefly, the fusion protein GST-proHNP1 was expressed in *E. coli* BL21 with IPTG induction. The insoluble inclusion bodies were denatured by 8 M urea and then folded in 2 M urea, 3 mM cysteine and 0.3 mM cystine. The folded fusion protein was dialyzed in a pH 7 buffer containing 20 mM Tris-HCl, 150 mM NaCl and 1.5 mM $CaCl_2$. The fusion protein was then cleaved by thrombin, producing proHNP1, which was purified by reversed-phase HPLC. ProHNP1 was further cleaved by cyanogen bromide to yield the correctly folded HNP-1. The crude HNP-1 was purified by reversed-phase HPLC and analyzed by electrospray ionization mass spectrometry to confirm the mass (3634 Da). The yield of HNP-1 was ~3 mg per liter culture. Antimicrobial assays confirmed the activity of the protein. For example, 100% killing of *S. aureus* is reached at 64 μg/ml HNP-1.

Microcrystalline HNP-1 was precipitated from a polyethylene glycol 400 (PEG-400) solution containing 30 mM cacodylate and 60 mM Li_2SO_4 at pH 6.5. The PEG-400 solution was added slowly to a protein stock solution to reach a final PEG-400 concentration of 30 wt %. Two protein stock solutions, at concentrations of 30 mg/ml and 36 mg/ml, were used. The protein precipitants were centrifuged in a sealed pipette tip, the supernatant removed, the pipette tip

cut open, and the precipitant was centrifuged into a 4 mm MAS rotor. Two HNP-1 samples, one in a 4 mm MAS rotor containing ~4 mg protein and the other in a 2.5 mm MAS rotor (~2.7 mg protein) were used in this study.

Solid-state NMR spectroscopy

Most SSNMR experiments were carried out on a Bruker AVANCE-600 (14.1 Tesla) spectrometer (Karlsruhe, Germany) using triple-resonance MAS probes. Most spectra were measured at 253 – 268 K under MAS frequencies of 8 – 15 kHz. 2D CM_5RR spectra were acquired on a 900 MHz NMR spectrometer at the Harvard/MIT Center for Magnetic Resonance. The 900 MHz spectra were measured on a 2.5 mm MAS probe under 20 kHz MAS.

Typical radio-frequency (rf) pulse lengths were 3.5 μs for ^{13}C, 6.0 μs for ^{15}N, and 2.5-4.0 μs for ^{1}H. ^{1}H decoupling fields were typically 70 kHz on the 4 mm rotor sample and 100 kHz on the 2.5 mm rotor sample. ^{13}C chemical shifts were referenced externally to the α-Gly ^{13}CO signal at 176.49 ppm on the TMS scale, and ^{15}N chemical shifts were referenced to the ^{15}N signal of N-acetylvaline at 122.0 ppm on the liquid ammonia scale. The TMS scale differs from the DSS scale by 1.7 ppm, thus all ^{13}C chemical shift values reported here should be increased by 1.7 ppm before comparing with DSS-referenced solution NMR chemical shifts. For torsion angle prediction by the TALOS software, we converted the TMS-based chemical shifts to DSS-referenced values.

2D ^{13}C-^{13}C dipolar-assisted rotational resonance (DARR) experiments [53] were acquired under 8 kHz MAS on the 4 mm rotor sample and 10-15 kHz on the 2.5 mm rotor sample. Four spectra were acquired with mixing times of 20 ms, 40 ms, 100 ms, and 200 ms. For the 4 mm rotor sample, the maximum evolution time for the indirect dimension was 5.6 ms, corresponding to 300 t_1 points. The number of scans per t_1 slice was 96 and the recycle delay was 2 s, giving an experimental time of ~16 hour per 2D spectrum. For the 2.5 mm rotor sample, the maximum ^{13}C evolution time was increased to 7.2 – 7.4 ms due to the better homogeneity and spectral resolution of the sample. 380 t_1 points were measured for the 20 ms and 40 ms experiments and 580 t_1 points were measured for the 100 ms and 200 ms mixing times. The experimental time was 18 – 26 hours per 2D spectrum.

Sequence-specific ^{13}C and ^{15}N resonance assignment was carried out by 3D NCOCX and NCACX experiments [34; 35; 54] under 8 kHz MAS at 268 K. Magnetization transfer between ^{15}N and ^{13}CO or ^{15}N and $^{13}C\alpha$ was achieved using band-selective SPECIFIC-CP [55]. In the intra-residue NCACX experiment, the Cα magnetization was selected by a 17-kHz ^{15}N spin-lock field and a 25-kHz ^{13}C spin lock field on resonance with Cα. In the inter-residue NCOCX experiment, the spin-lock fields were 27 kHz for ^{15}N and 30 kHz for ^{13}C on resonance with Cα. In the latter case, since the CO offset was 18 kHz, the effective field of the CO resonances was ~35 kHz, thus satisfying the sideband matching condition with ^{15}N. After SPECIFIC-CP, ^{13}C-^{13}C magnetization transfer occurred during a DARR mixing time, which was 40 ms for NCACX and 60 ms for NCOCX.

For the NCOCX experiment, the ^{15}N spectral width was 4 kHz and the maximum t_1 evolution time was 4.75 ms, corresponding to 38 t_1 points. The ^{13}CO spectral width was 2 kHz and the number of t_2 points was 22, giving a maximum t_2 of 5.56 ms. The experimental time was about 2.5 days. For the NCACX experiment, the ^{15}N spectral width was the same as that of NCOCX, while the $^{13}C\alpha$ (ω_2) spectral width was 4.5 kHz and the acquisition time was 5.56 ms, corresponding to 50 t_2 points. The experimental time was 2 days.

The 2D ^{15}N-^{15}N correlation experiment was conducted using ^{1}H-driven spin diffusion (PDSD) under 6 kHz MAS at 253 K. The mixing time was 3 s to obtain inter-residue ^{15}N-^{15}N correlation peaks. The indirect dimension has a spectral width of 16 kHz and an acquisition time of 6.88

ms, corresponding to 220 t_1 points. The number of scan per t_1 slice was 144 and the recycle delay was 1.5 s, giving an experimental time of 40 hours.

The N-H doubled HNCH experiment to determine φ torsion angles [36; 47] were carried out on the 2.5 mm rotor sample under 8 kHz MAS at 263 K. ^{1}H homonuclear decoupling during the N-H and C-H evolution periods were achieved using the FSLG sequence [56]. The Cα peaks of the chemical shift dimension were assigned based on the 2D and 3D correlation spectra. Although resonance overlap was unavoidable, most residues have consistent φ angles between the TALOS and the crystal structure results, thus allowing the residues of interest to be measured. For sensitivity reasons, only the intensities at 0 and half a rotor period of dipolar evolution times were measured. Simulations (Figure S4) indicate that the intensity at half a rotor period is the most sensitive to φ angle variations.

Structure calculation

The ^{13}Cα, ^{13}Cβ, ^{13}CO and ^{15}N chemical shifts were inputted into the TALOS program [46] to obtain (φ, ψ) torsion angles. Structure calculations were performed using the simulated annealing protocol of the XPLOR-NIH program [57; 58]. Input constraints included 60 torsion angles, 9 distances associated with the disulfide bonds, 46 distances between sequential residues, and 24 non-sequential inter-residue distances. An ensemble of 200 structures were first calculated by performing molecular dynamics at 3500 K for 40 ps, followed by slow cooling from 3500 K to 25 K in 12.5 K steps. At each temperature 0.4 ps of dynamics was performed using a soft square NOE potential. Each structure was then refined with the same protocol but with 10 ps of initial annealing using a hard square potential with the k_{NOE} force constant held at 30 kcal. After refinement, the 10 lowest-energy structures were chosen to represent the final structure of HNP-1. All structures were visualized in Chimera (UCSF).

Accession numbers

The HNP-1 SSNMR structure coordinates have been deposited in the Protein Data Bank (PDB code: 2KHT). The chemical shifts and distance restraints have been deposited in the Biological Magnetic Resonance Bank (accession number: rcsb101138).

Supplementary Material

Refer to Web version on PubMed Central for supplementary material.

Acknowledgments

The authors thank Chih-Chia Su for assistance with microcrystal visualization, Professor Chad Rienstra for sharing the design of microcrystal transfer tools, Professor Robert Griffin, Dr. Jozef Lewandowski, Dr. Gaël De Paëpe and Dr. Tony Bielecki for assistance with the 900 MHz NMR experiments, and Dr. Andrew Severin and Dr. Shenhui Li for help with the XPLOR-NIH structure calculations.

This work is supported by the NIH grant GM66976 to M.H. and P41-EB-002026 for the 900 MHz NMR time at MIT.

References

1. Selsted ME, Ouellette AJ. Mammalian defensins in the antimicrobial immune response. Nat. Immunol 2005;6:551–557. [PubMed: 15908936]
2. Ganz T, Selsted ME, Szklarek D, Harwig SS, Daher K, Bainton DF, Lehrer RI. Defensins. Natural peptide antibiotics of human neutrophils. J. Clin. Invest 1985;76:1427–1435. [PubMed: 2997278]
3. Hill CP, Yee J, Selsted ME, Eisenberg D. Crystal structure of defensin HNP-3, an amphiphilic dimer: mechanisms of membrane permeabilization. Science 1991;251:1481–1485. [PubMed: 2006422]
4. Szyk A, Wu Z, Tucker K, Yang D, Lu W, Lubkowski J. Crystal structures of human alpha-defensins HNP4, HD5, and HD6. Protein Sci 2006;15:2749–60. [PubMed: 17088326]

5. Gabay JE, Scott RW, Campanelli D, Griffith J, Wilde C, Marra MN, Seeger M, Nathan CF. Antibiotic proteins of human polymorphonuclear leukocytes. Proc. Natl. Acad. Sci. U. S. A 1989;86:5610–5614. [PubMed: 2501794]
6. Jones DE, Bevins CL. Defensin-6 mRNA in human Paneth cells: implications for antimicrobial peptides in host defense of the human bowel. FEBS Lett 1993;315:187–192. [PubMed: 8417977]
7. Jones DE, Bevins CL. Paneth cells of the human small intestine express an antimicrobial peptide gene. J. Biol. Chem 1992;267:23216–23225. [PubMed: 1429669]
8. Ericksen B, Wu Z, Lu W, Lehrer RI. Antibacterial activity and specificity of the six human {alpha}-defensins. Antimicrob. Agents Chemother 2005;49:269–275. [PubMed: 15616305]
9. Wu Z, Ericksen B, Tucker K, Lubkowski J, Lu W. Synthesis and characterization of human alpha-defensins 4-6. J. Pept. Res 2004;64:118–125. [PubMed: 15317502]
10. Lehrer RI, Lichtenstein AK, Ganz T. Defensins: antimicrobial and cytotoxic peptides of mammalian cells. Annu. Rev. Immunol 1993;11:105–128. [PubMed: 8476558]
11. Ganz T. Defensins: antimicrobial peptides of innate immunity. Nat. Rev. Immunol 2003;3:710–720. [PubMed: 12949495]
12. Hong M. Structure, topology, and dynamics of membrane peptides and proteins from solid-state NMR spectroscopy. J. Phys. Chem. B 2007;111:10340–10351. [PubMed: 17685648]
13. Doherty T, Waring AJ, Hong M. Dynamic structure of disulfide-removed linear analogs of tachyplesin-I in the lipid bilayer from solid-state NMR. Biochemistry 2008;47:1105–1116. [PubMed: 18163648]
14. Doherty T, Waring AJ, Hong M. Membrane-bound conformation and topology of the antimicrobial peptide tachyplesin-I by solid-state NMR. Biochemistry 2006;45:13323–13330. [PubMed: 17073453]
15. Mani R, Cady SD, Tang M, Waring AJ, Lehrer RI, Hong M. Membrane-dependent oligomeric structure and pore formation of a b-hairpin antimicrobial peptide in lipid bilayers from solid-state NMR. Proc. Natl. Acad. Sci. USA 2006;103:16242–16247. [PubMed: 17060626]
16. Mani R, Tang M, Wu X, Buffy JJ, Waring AJ, Sherman MA, Hong M. Membrane-bound dimer structure of a b-hairpin antimicrobial peptide from rotational-echo double-resonance solid-state NMR. Biochemistry 2006;45:8341–8349. [PubMed: 16819833]
17. Tang M, Waring AJ, Hong M. Mechanism of Arg insertion into lipid membranes and pore formation by a cationic peptide. J. Am. Chem. Soc 2007;129:11438–11446. [PubMed: 17705480]
18. Tang M, Waring AJ, Lehrer RI, Hong M. Effects of Guanidinium-Phosphate Hydrogen Bonding on the Membrane-Bound Structure and Activity of an Arginine-Rich Membrane Peptide from Solid-State NMR. Angew. Chem. Int. Ed. Engl 2008;47:3202–3205. [PubMed: 18338418]
19. Tang M, Waring AJ, Lehrer RI, Hong M. Orientation of a b-hairpin Antimicrobial Peptide in Lipid Bilayers from 2D Dipolar Chemical-Shift Correlation NMR. Biophys. J 2006;90:3616–3624. [PubMed: 16500957]
20. Buffy JJ, Hong T, Yamaguchi S, Waring A, Lehrer RI, Hong M. Solid-State NMR Investigation of the Depth of Insertion of Protegin-1 in Lipid Bilayers Using Paramagnetic Mn2+ Biophys. J 2003;85:2363–2373. [PubMed: 14507700]
21. Buffy JJ, McCormick MJ, Wi S, Waring A, Lehrer RI, Hong M. Solid-State NMR Investigation of the Selective Perturbation of Lipid Bilayers by the Cyclic Antimicrobial Peptide RTD-1. Biochemistry 2004;43:9800–9812. [PubMed: 15274634]
22. Kagan BL, Selsted ME, Ganz T, Lehrer RI. Antimicrobial defensin peptides form voltage-dependent ion-permeable channels in planar lipid bilayer membranes. Proc. Natl. Acad. Sci. U. S. A 1990;87:210–214. [PubMed: 1688654]
23. Wimley WC, Selsted ME, White SH. Interactions between human defensins and lipid bilayers: evidence for formation of multimeric pores. Protein Sci 1994;3:1362–1373. [PubMed: 7833799]
24. Lohner K, Latal A, Lehrer RI, Ganz T. Differential scanning microcalorimetry indicates that human defensin, HNP-2, interacts specifically with biomembrane mimetic systems. Biochemistry 1997;36:1525–1531. [PubMed: 9063901]
25. Castellani FR,B, Diehl A, Schubert M, Rehbein K, Oschkinat H. Structure of a protein determined by solid-state magic-angle-spinning NMR spectroscopy. Nature 2002;420:98–102. [PubMed: 12422222]

26. Igumenova T, Wand A, McDermott A. Assignment of the backbone resonances for microcrystalline ubiquitin. J Am Chem Soc 2004;126:5323–31. [PubMed: 15099118]
27. Franks W, Zhou D, Wylie B, Money B, Graesser D, Frericks H, Sahota G, Rienstra C. Magic-angle spinning solid-state NMR spectroscopy of the beta1 immunoglobulin binding domain of protein G (GB1): 15N and 13C chemical shift assignments and conformational analysis. J. Am. Chem. Soc 2005;127:12291–12305. [PubMed: 16131207]
28. Marulanda D, Tasayco M, Cataldi M, Arriaran V, Polenova T. Resonance assignments and secondary structure analysis of E. coli thioredoxin by magic angle spinning solid-state NMR spectroscopy. J. Phys. Chem. B 2005;109:18135–45. [PubMed: 16853329]
29. Petkova AT, Ishii Y, Balbach JJ, Antzutkin ON, Leapman RD, Delaglio F, Tycko R. A structural model for Alzheimer's beta -amyloid fibrils based on experimental constraints from solid state NMR. Proc. Natl. Acad. Sci. USA 2002;99:16742–7. [PubMed: 12481027]
30. Wasmer C, Lange A, Van Melckebeke H, Siemer AB, Riek R, Meier BH. Amyloid fibrils of the HET-s(218-289) prion form a beta solenoid with a triangular hydrophobic core. Science 2008;319:1523–1526. [PubMed: 18339938]
31. Helmus JJ, Surewicz K, Nadaud PS, Surewicz WK, Jaroniec CP. Molecular conformation and dynamics of the Y145Stop variant of human prion protein in amyloid fibrils. Proc. Natl. Acad. Sci. U. S. A 2008;105:6284–6289. [PubMed: 18436646]
32. Cady SD, Hong M. Amantadine-Induced Conformational and Dynamical Changes of the Influenza M2 Transmembrane Proton Channel. Proc. Natl. Acad. Sci. U.S.A 2008;105:1483–1488. [PubMed: 18230730]
33. Lange A, Giller K, Hornig S, Martin-Eauclaire MF, Pongs O, Becker S, Baldus M. Toxin-induced conformational changes in a potassium channel revealed by solid-state NMR. Nature 2006;440:959–962. [PubMed: 16612389]
34. Hong M. Resonance Assignment of 13C/15N Labeled Proteins by Two- and Three-Dimensional Magic-Angle-Spinning NMR. J. Biomol. NMR 1999;15:1–14. [PubMed: 10549131]
35. Rienstra CM, Hohwy M, Hong M, Griffin RG. 2D and 3D 15N-13C-13C NMR chemical shift correlation spectroscopy of solids: assignment of MAS spectra of peptides. J. Am. Chem. Soc 2000;122:10979–10990.
36. Hong M, Gross JD, Griffin RG. Site-resolved determination of peptide torsion angle phi from the relative orientations of backbone N-H and C-H bonds by solid-state NMR. J. Phys. Chem. B 1997;101:5869–5874.
37. Costa PR, Gross JD, Hong M, Griffin RG. Solid-State NMR Measurement of psi in Peptides: a NCCN 2Q-Heteronuclear Local Field Experiment. Chem. Phys. Lett 1997;280:95–103.
38. Feng X, Eden M, Brinkmann A, Luthman H, Eriksson L, Graslund A, Antzutkin ON, Levitt MH. Direct determination of a peptide torsion angle psi by double-quantum solid-state NMR. J. Am. Chem. Soc 1997;119:12006–12007.
39. Jaroniec CP, Tounge BA, Rienstra CM, Herzfeld J, Griffin RG. Measurement of 13C-15N distances in uniformly 13C labeled biomolecules: J-decoupled REDOR. J. Am. Chem. Soc 1999;121:10237–10238.
40. Wei G, de Leeuw E, Pazgier M, Yuan W, Zou G, Wang J, Ericksen B, Lu WY, Lehrer RI, Lu W. Through the looking glass: Mechanistic insights from enantiomeric human defensins. J. Biol. Chem. 2009 Epub ahead of print.
41. Hohwy M, Jakobsen HJ, Eden M, Levitt MH, Nielsen NC. Broadband dipolar recoupling in the nuclear magnetic resonance of rotating solids: a compensated C7 pulse sequence. J. Chem. Phys 1998;108:2686–2694.
42. De Paëpe G, Bayro MJ, Lewandowski J, Griffin RG. Broadband homonuclear correlation spectroscopy at high magnetic fields and MAS frequencies. J. Am. Chem. Soc 2006;128:1776–1777. [PubMed: 16464061]
43. Kornhaber GJ, Snyder D, Moseley HN, Montelione GT. Identification of zinc-ligated cysteine residues based on 13Calpha and 13Cbeta chemical shift data. J. Biomol. NMR 2006;34:259–269. [PubMed: 16645816]
44. Sharma D, Rajarathnam K. 13C NMR chemical shifts can predict disulfide bond formation. J. Biomol. NMR 2000;18:165–171. [PubMed: 11101221]

45. Wishart DS, Sykes BD, Richards FM. Relationship between nuclear magnetic resonance chemical shift and protein secondary structure. J. Mol. Biol 1991;222:311–333. [PubMed: 1960729]
46. Cornilescu G, Delaglio F, Bax A. Protein backbone angle restraints from searching a database for chemical shift and sequence homology. J. Biomol. NMR 1999;13:289–302. [PubMed: 10212987]
47. Hong M, Gross JD, Rienstra CM, Griffin RG, Kumashiro KK, Schmidt-Rohr K. Coupling Amplification in 2D MAS NMR and Its Application to Torsion Angle Determination in Peptides. J. Magn. Reson 1997;129:85–92. [PubMed: 9405219]
48. Huster D, Yamaguchi S, Hong M. Efficient beta-sheet identification in proteins by solid-state NMR spectroscopy. J. Am. Chem. Soc 2000;122:11320–11327.
49. Zech S, Wand A, McDermott A. Protein structure determination by high-resolution solid-state NMR spectroscopy: application to microcrystalline ubiquitin. J Am Chem Soc 2005;127:8618–26. [PubMed: 15954766]
50. Franks WT, Wylie BJ, Schmidt HL, Nieuwkoop AJ, Mayrhofer RM, Shah GJ, Graesser DT, Rienstra CM. Dipole tensor-based atomic-resolution structure determination of a nanocrystalline protein by solid-state NMR. Proc. Natl. Acad. Sci. U. S. A 2008;105:4621–4626. [PubMed: 18344321]
51. Pardi A, Zhang XL, Selsted ME, Skalicky JJ, Yip PF. NMR studies of defensin antimicrobial peptides. 2. Three-dimensional structures of rabbit NP-2 and human HNP-1. Biochemistry 1992;31:11357–11364. [PubMed: 1445873]
52. Lourenzoni MR, Namba AM, Caseli L, Degrève L, Zaniquelli ME. Study of the interaction of human defensins with cell membrane models: relationships between structure and biological activity. J. Phys. Chem. B 2007;111:11318–11329. [PubMed: 17784741]
53. Takegoshi K, Nakamura S, Terao T. ^{13}C - ^{1}H dipolar-assisted rotational resonance in magic-angle spinning NMR. Chem. Phys. Lett 2001;344:631–637.
54. Straus S, Bremi T, Ernst R. Experiments and strategies for the assignment of fully 13C/15N-labelled polypeptides by solid state NMR. J. Biomol. NMR 1998;12:39–50. [PubMed: 9729787]
55. Baldus M, Geurts DG, Hediger S, Meier BH. Efficient N-15-C-13 polarization transfer by adiabatic-passage Hartmann-Hahn cross polarization. J. M. R 1996;118:140–144.
56. Bielecki A, Kolbert AC, Levitt MH. Frequency-switched pulse sequences: homonuclear decoupling and dilute spin NMR in solids. Chem. Phys. Lett 1989;155:341–346.
57. Schwieters C, Kuszewski J, Tjandra N, Clore G. The Xplor-NIH NMR Molecular Structure Determination Package. J. Magn. Res 2003;160:66–74.
58. Schwieters C, Kuszewski J, Clore G. Using Xplor-NIH for NMR molecular structure determination. Progr. NMR Spectroscopy 2006;48:47–62.

Figure 1.
Amino acid sequence and disulfide bond connectivities of HNP-1.

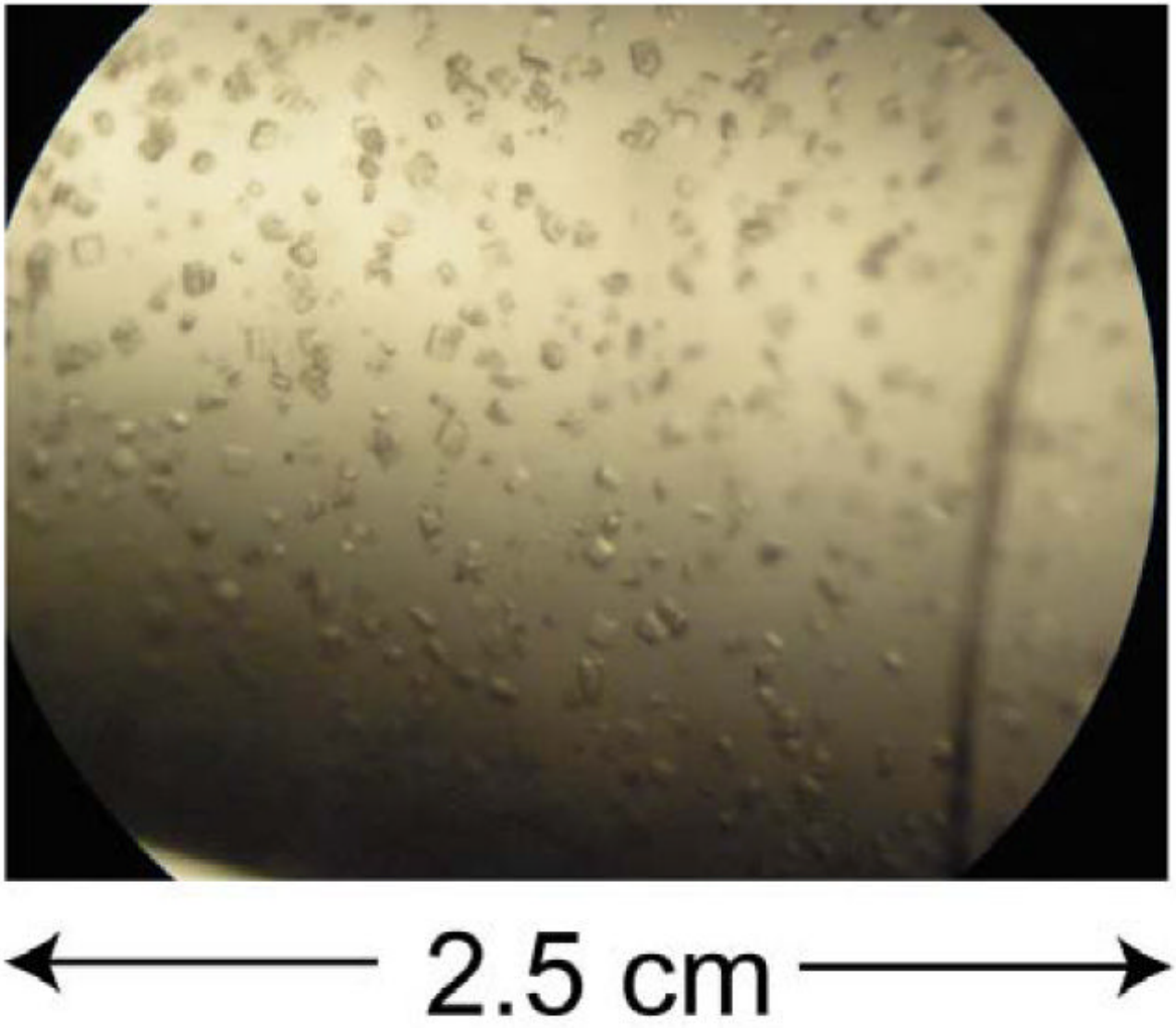

Figure 2.
An image of microcrystalline HNP-1. The average size of the crystals is ~20 μm.

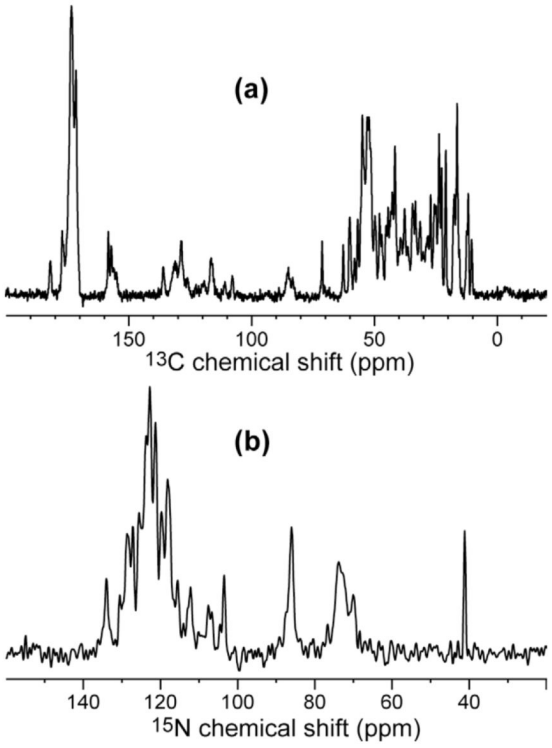

Figure 3.
1D CP-MAS spectra of microcrystalline U-^{13}C, ^{15}N-labeled HNP-1. (a) ^{13}C spectrum, measured at 258 K at a ^{13}C Larmor frequency of 225 MHz. (b) ^{15}N spectrum, measured at 268 K at a ^{15}N Larmor frequency of 60 MHz.

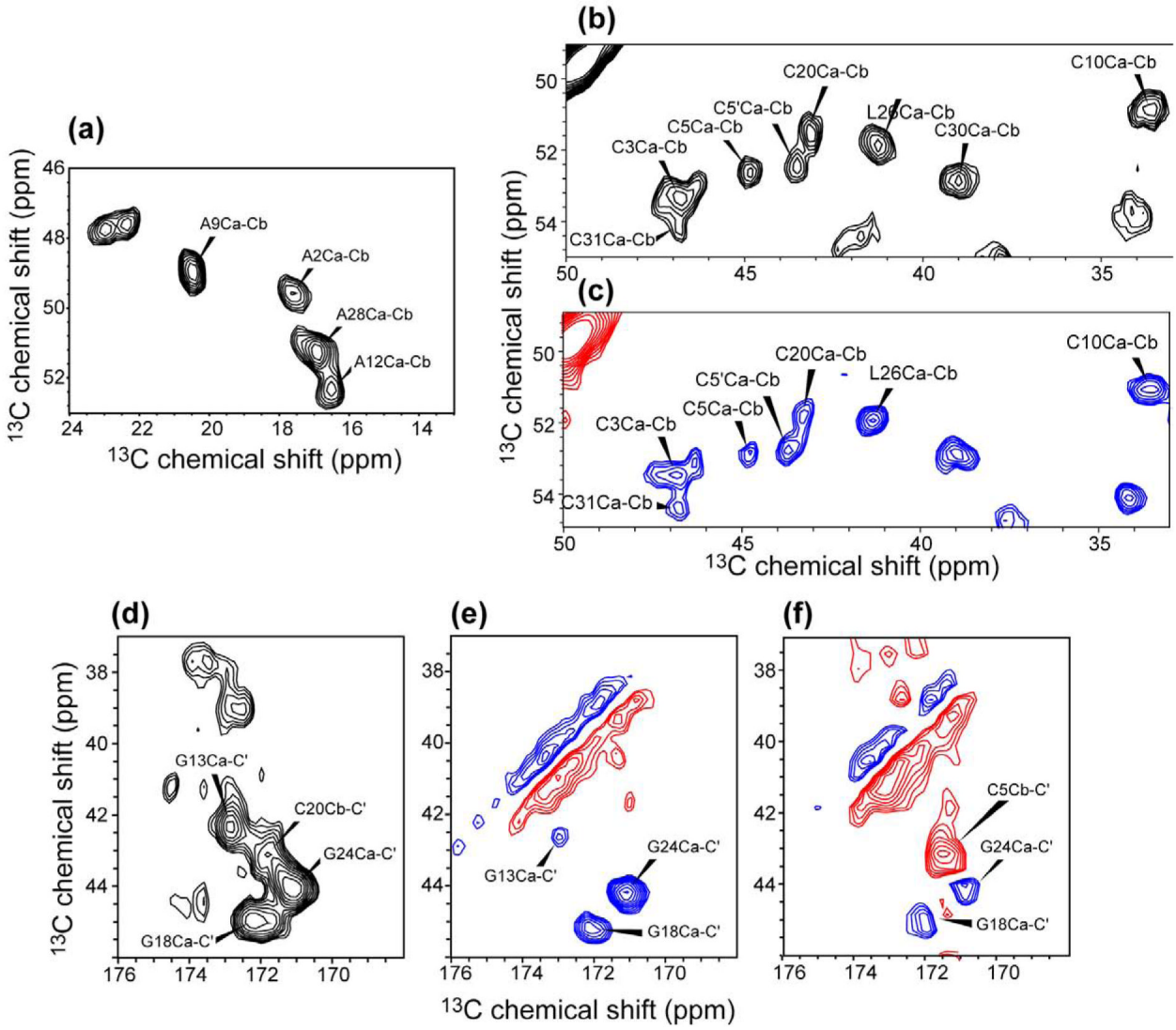

Figure 4.

Representative regions of 2D ^{13}C-^{13}C correlation spectra of HNP-1. (a) Ala Cα-Cβ region from a 40 ms DARR spectrum. (b) Cys Cα-Cβ region from a 40 ms DARR spectrum. (c) Cys Cα-Cβ region from a 0.8 ms CM_5RR spectrum. Blue: positive intensities. Red: negative intensities. (d-f) CO-Cα/Cβ region. (d) 40 ms DARR spectrum, (e) 0.8 ms CM_5RR spectrum. (f) 1.5 ms CM_5RR. The sign of the cross peak intensities distinguishes the one-bond Gly CO-Cα peaks (red, indicating negative) from the two-bond Cys CO-Cβ peaks (blue, indicating positive).

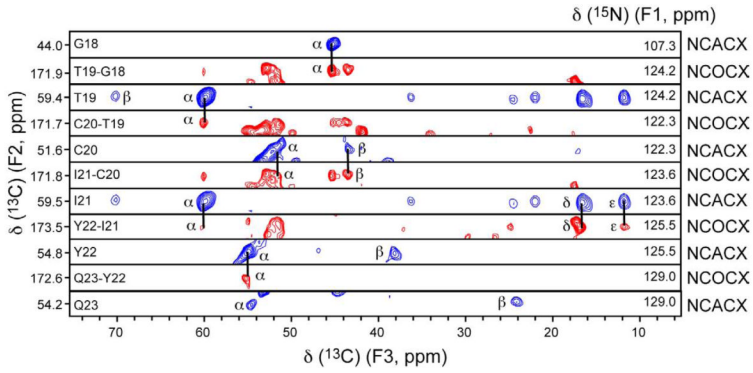

Figure 5.

F2-F3 strips of 3D NCACX (blue) and NCOCX (red) spectra for residues G18 to Q23, illustrating sequential resonance assignment. The strip width for the F2 dimension is 2.3 ppm. The F1 ^{15}N chemical shifts for the strips are indicated on the right end of each strip.

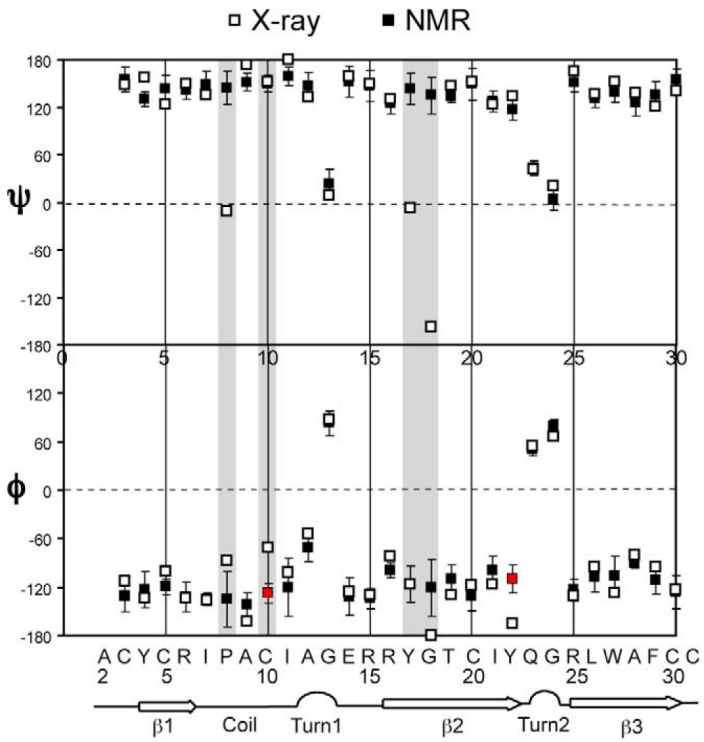

Figure 6.

HNP-1 (φ, ψ) torsion angles determined from solid-state NMR ^{13}C and ^{15}N chemical shifts (filled squares). The torsion angles of HNP-3 are shown for comparison (open squares and ribbons) (PDB accession code: 1DFN). Residues with significantly different torsion angles from the crystal structure values of HNP-3 are shaded.

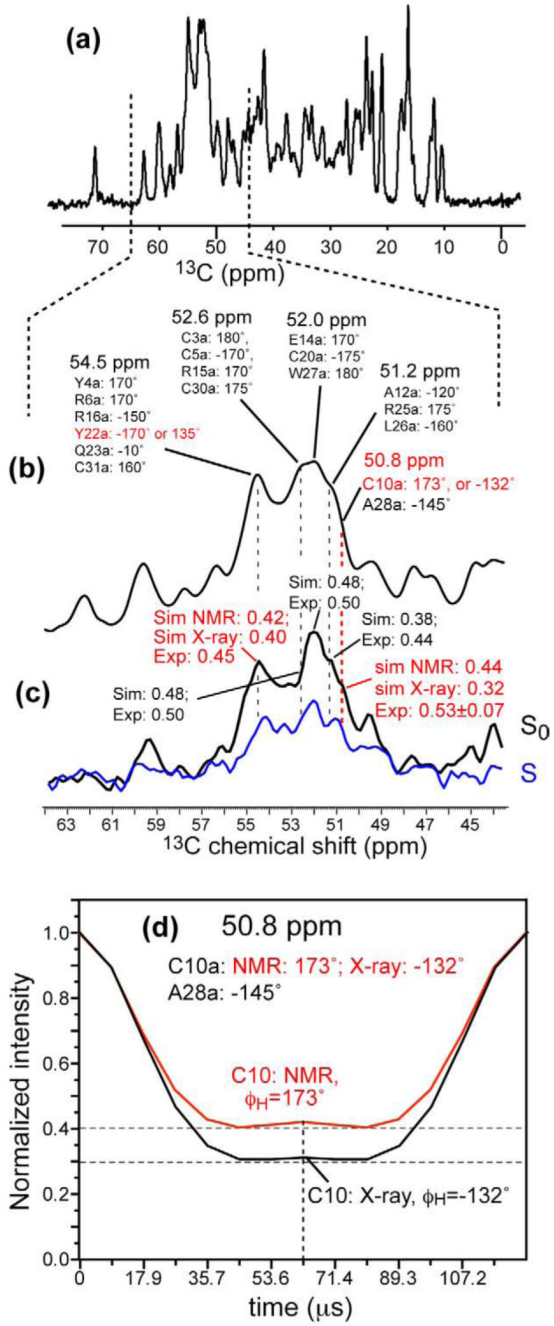

Figure 7.

Direct measurement of φ torsion angles by HNCH. (a) Aliphatic region of the 1D ^{13}C spectrum. (b) Cα region (44-64 ppm) of the ^{13}C spectrum, indicating the assignment of the resolved peaks and the φ_H torsion angles (φ_H+60°=φ) of each residue. For most residues the φ_H angles agree between TALOS and the crystal structure within ±10°. But for C10 and Y22, significant deviations exist. (c) Measured HNCH spectra with dipolar evolution time of 0 (S_0) and half a rotor period (S, shown in blue). The measured $S.S_0$ values are indicated along with calculated values. The 50.8-ppm peak has an S/S_0 value that is consistent with the chemical shift derived φ angles and not the HNP-3 value. (d) Calculated HNCH curves for the 50.8 ppm C10/A28 Cα peak. The A28 φ_H angle is fixed while the C10 φ_H angle is either 173° or 132°. The measured

HNCH intensity at the middle of the rotor period is consistent with the TALOS φ_H angle but not the crystal structure value.

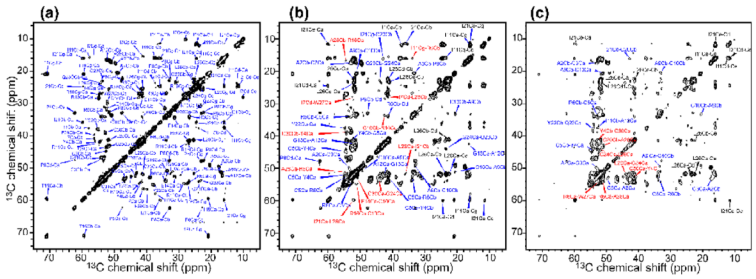

Figure 8.

2D ^{13}C-^{13}C DARR spectra of HNP-1 with mixing times (a) 40 ms, (b) 100 ms, and (c) 200 ms. In (a), all peaks are assigned. In (b) and (c), only inter-residue and intra-residue multiple-bond correlations not observed in (a) are assigned. Red: non-sequential inter-residue correlations; blue: sequential correlations; black: intra-residue multiple-bond correlations.

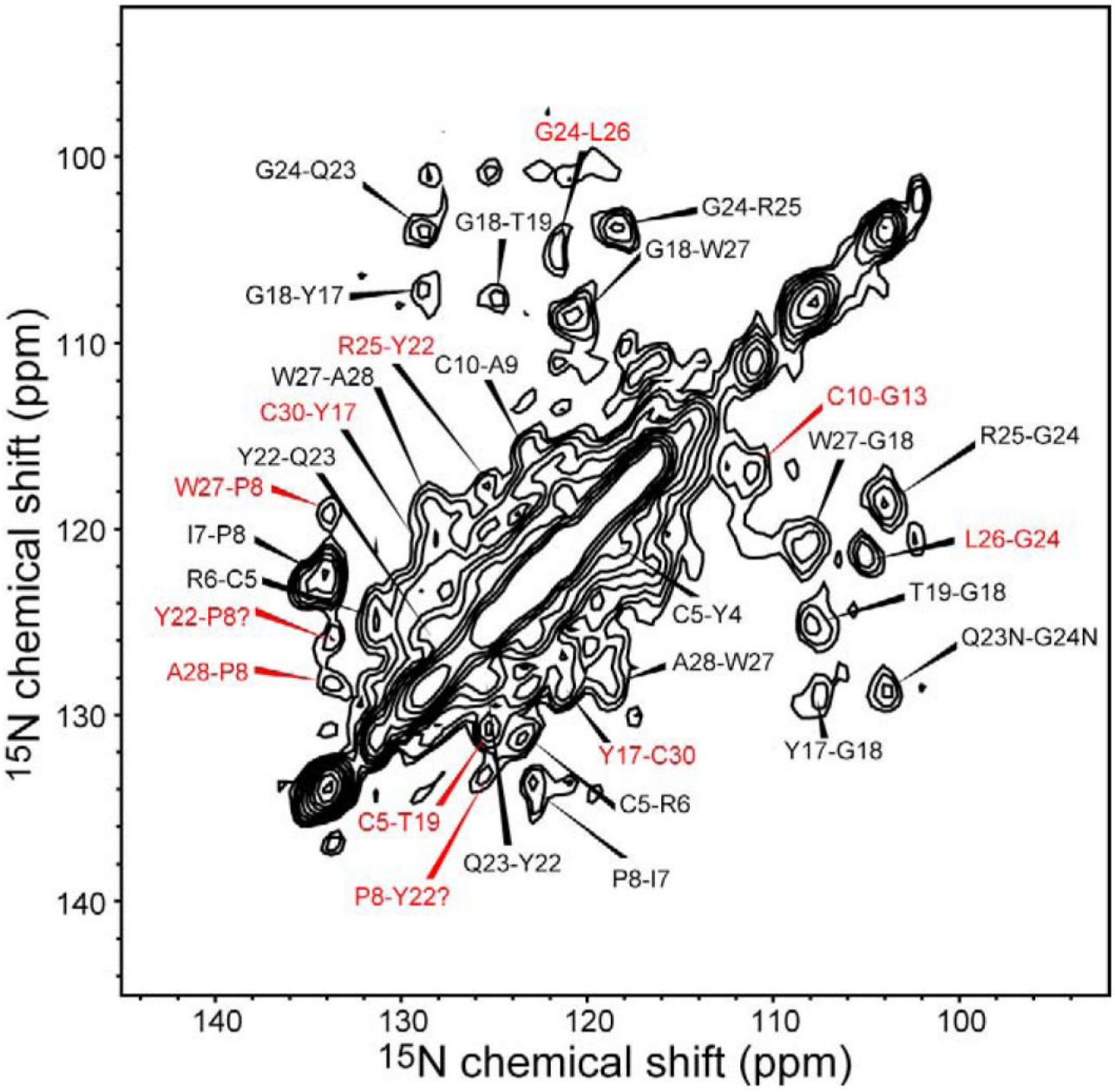

Figure 9.
^{15}N-^{15}N 2D PDSD spectrum with a mixing time of 3 s. Black and red assignments indicate sequential and non-sequential correlations, respectively.

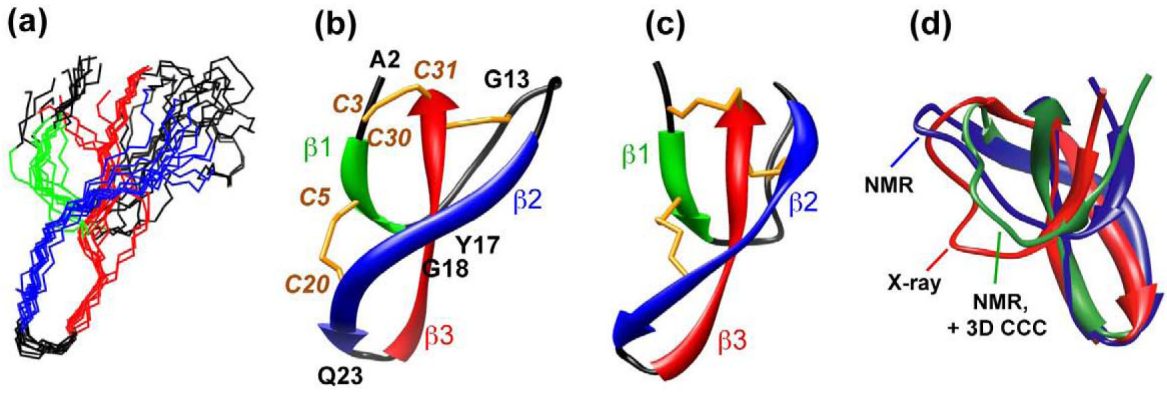

Figure 10.

SSNMR structures of HNP-1 compared with the X-ray crystal structure of HNP-3. (a) Eleven minimum energy SSNMR structures of HNP-1. (b) Average structure of (a). (c) Crystal structure of HNP-3. The disulfide bonds are shown in orange. (d) Comparison of the β1-β2 loop conformation between the crystal structure (red), the current solid-state NMR structure (blue), and the NMR structure with the additional distance restraints from the 3D CCC experiment (green).

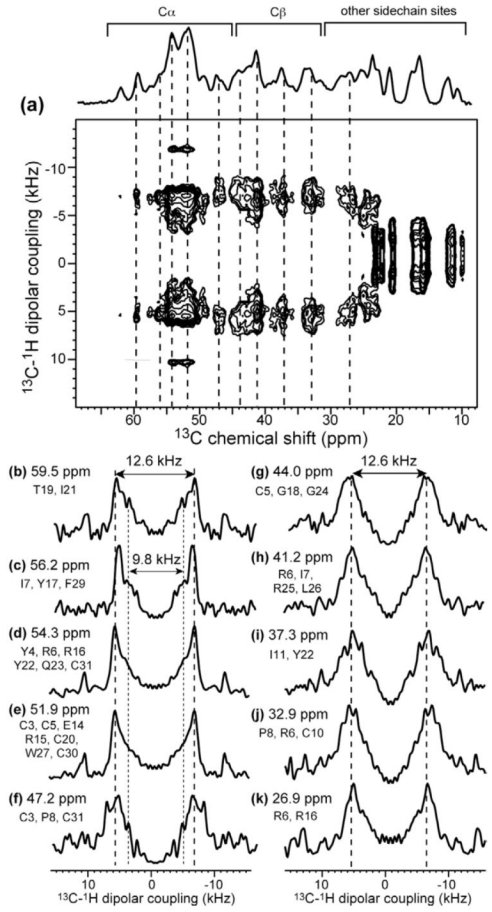

Figure 11.

2D ^{13}C-^{1}H LG-CP spectrum to determine the mobility of microcrystalline HNP-1. (a) 2D spectrum, measured under 11 kHz MAS and 293 K. (b-k) 1D dipolar cross sections at selected chemical shifts. Most Cα and Cβ cross sections show rigid-limit values (after taking into account the LG scaling factor of 0.577), except for the 56.2-ppm cross section (c), which has a second coupling that is smaller than the rest.

Table 1

^{13}C and ^{15}N chemical shifts of microcrystalline HNP-1 without lipids [a].

	N	Cα	Cβ	Cγ	Cδ	Cε	CO
A2	41.7	49.5	17.5				171.0
C3$^{(C31)}$ [b]	117.8	53.0	46.6				171.4
Y4	117.6	54.8					172.6
C5 $^{(C20)}$	130.6	52.7	44.5/43.4				171.4
R6	123.1	53.9	33.7	26.7	41.5		173.6
I7	122.3	56.5	41.2	28.0	15.3	10.1	172.6
P8	134.4	62.2	32.9	23.1/22.1	47.5		172.7
A9	122.6	48.8	20.6				172.9
C10$^{(C30)}$	115.6	50.8	33.4				173.0
I11	115.4	57.9	37.5	23.8	15.9	12.2	173.0
A12	121.9	51.8	16.6				175.2
G13	109.6	42.6					
E14	121.3	52.2	31.4	34.4	181.8		173.6
R15	130.6	52.7					171.4
R16	122.8	54.5	28.1	27.0	42.4	157.1	175.3
Y17	128.1	56.3	38.5	131.5			173.5
G18	107.3	45.0					171.9
T19	124.2	59.4	69.6	21.7			171.7
C20$^{(C5)}$	122.3	51.6	43.0				171.8
I21	123.6	59.5	35.8	24.3	16.2	11.4	173.5
Y22	125.5	54.8	37.7				172.6
Q23	129.0	54.2	23.8	31.9	176.5		173.9
G24	103.4	44.0					170.3
R25	118.4	51.6	32.2	25.5	41.2		172.0
L26	120.2	51.6	41.2	25.4	23.2	22.4	174.4
W27	120.7	52.0	29.0				175.3
A28	127.1	51.0	16.9				172.8
F29	123.8	56.6	39.8	129.2			

	N	Cα	Cβ	Cγ	Cδ	Cε	CO
C30(C10)	121.9	53.0	38.6				172.7
C31(C3)	121.1	55.3	47.0				177.5

[a]The ^{13}C chemical shifts are referenced to TMS. To convert to DSS-referenced chemical shifts, the ^{13}C frequencies in this table should be increased by 1.7 ppm. The ^{15}N chemical shifts are referenced to liquid ammonia.

[b]The partner cysteine involved in the disulfide bond is indicated in the bracket.

Table 2

Non-sequential inter-residue distance restraints.

residues	spectrum	type of correlation	Distance (A)
C10Cα-E14Cβ	40 ms DARR	medium range: i – (i+4)	2.5 – 4.8
E14Cγ-C30Cα	40 ms DARR	long range	2.5 – 4.8
A2Cα-C30Cα	100 ms DARR	long range: β1 – β3	2.5 – 5.4
Y4Cα-C30Cβ	100 ms DARR	long range: β1 – β3	2.5 – 5.4
R6Cα-A28Cα	100 ms DARR	long range: β1 – β3	2.5 – 5.4
I7Cγ-L26Cβ	100 ms DARR	long range	2.5 – 5.4
I7Cγ-W27Cα	100 ms DARR	long range	2.5 – 5.4
C10Cβ-R16Cδ	100 ms DARR	long range	2.5 – 5.4
R16Cα-A28Cβ	100 ms DARR	long range: β2 – β3	2.5 – 5.4
I21Cα-L26Cα	100 ms DARR	long range: β2 – β3	2.5 – 5.4
R6Cδ-C30Cβ	200 ms DARR	long range: β1 – β3	2.5 – 6.3
R16Cβ-F29Cα	200 ms DARR	long range: β2 – β3	2.5 – 6.3
R6Cγ-A28Cα	200 μs CHHC	long range: β1 – β3	2.5 – 8.0
C5Cβ-F29Cβ	300 μs CHHC	long range: β1 – β3	2.5 – 8.0
Y4N-G13N	3 s ^{15}N PDSD	long range	3.0 – 6.0
C5N-T19N	3 s ^{15}N PDSD	long range: β1 – β2	3.0 – 6.0
P8N-Y22N	3 s ^{15}N PDSD	long range	3.0 – 6.0
P8N-W27N	3 s ^{15}N PDSD	long range	3.0 – 6.0
P8N-A28N	3 s ^{15}N PDSD	long range	3.0 – 6.0
C10N-G13N	3 s ^{15}N PDSD	medium range: i – (i+3)	3.0 – 6.0
Y17N-C30N	3 s ^{15}N PDSD	long range: β2 – β3	3.0 – 6.0
G18N-W27N	3 s ^{15}N PDSD	long range: β2 – β3	3.0 – 6.0
Y22N-R25N	3 s ^{15}N PDSD	medium range: β2 – β3	3.0 – 6.0
G24N-L26N	3 s ^{15}N PDSD	medium range: i – (i+2)	3.0 – 6.0

Table 3

Structure calculation summary of HNP-1.

Restraints	
Total inter-residue CC and NN restraints	60
Sequential (|i-j| = 1)	36
Medium range (1< |i-j| <4)	4
Long range (|i-j| > 4)	20
β1 – β3	6
β2 – β3	6
β1 – β2	1
CC Restraints in the class 2.5 – 4.8 Å	4
CC Restraints in the class 2.5 – 5.4 Å	18
CC Restraints in the class 2.5 – 6.3 Å	5
CC Restraints in the class 2.5 – 8.0 Å	7
NN restraints in the class 2.5 – 4.0 Å	10
NN restraints in the class 3.0 – 6.0 Å	10
Total (φ, ψ) torsional angle restraints	56
rms deviation of 11 lowest-energy structures from the crystal structure	
Backbone atoms:	2.7 Å
Heavy atoms:	3.8 Å
E_{global}(kcal mol^{-1})	264